

## Rheology of a dilute suspension of liquid-filled elastic capsules

Prosenjit Bagchi\* and R. Murthy Kalluri

*Department of Mechanical and Aerospace Engineering, Rutgers University, The State University of New Jersey, Piscataway, New Jersey 08854, USA*

(Received 6 March 2010; published 25 May 2010)

Rheology of a dilute suspension of liquid-filled elastic capsules in linear shear flow is studied by three-dimensional numerical simulations using a front-tracking method. This study is motivated by a recent discovery that a suspension of viscous vesicles exhibits a shear viscosity minimum when the vesicles undergo an unsteady vacillating-breathing dynamics at the threshold of a transition between the tank-treading and tumbling motions. Here we consider capsules of spherical resting shape for which only a steady tank-treading motion is observed. A comprehensive analysis of the suspension rheology is presented over a broad range of viscosity ratio (ratio of internal-to-external fluid viscosity), shear rate (or, capillary number), and capsule surface-area dilatation. We find a result that the capsule suspension exhibits a shear viscosity minimum at moderate values of the viscosity ratio, and high capillary numbers, even when the capsules are in a steady tank-treading motion. It is further observed that the shear viscosity minimum exists for capsules with area-dilating membranes but not for those with nearly incompressible membranes. Nontrivial results are also observed for the normal stress differences which are shown to decrease with increasing capillary number at high viscosity ratios. Such nontrivial results neither can be predicted by the small-deformation theory nor can be explained by the capsule geometry alone. Physical mechanisms underlying these results are studied by decomposing the particle stress tensor into a contribution due to the elastic stresses in the capsule membrane and a contribution due to the viscosity differences between the internal and suspending fluids. It is shown that the elastic contribution is shear-thinning, but the viscous contribution is shear thickening. The coupling between the capsule geometry and the elastic and viscous contributions is analyzed to explain the observed trends in the bulk rheology.

DOI: [10.1103/PhysRevE.81.056320](https://doi.org/10.1103/PhysRevE.81.056320)

PACS number(s): 47.63.-b, 47.61.Jd, 87.16.D-, 47.57.-s

### I. INTRODUCTION

Blood is a multiphase suspension of deformable particulates. Erythrocytes or red blood cells constitute the primary particulate component of blood. They are easily deformable by fluid shear, and responsible for complex rheological behavior of blood. Understanding rheology of blood is a fundamental problem of immense biological importance and has been a subject of *in vivo* and *in vitro* studies over nearly a century (see, e.g., [1] for a review). These studies have addressed blood rheology on a macroscale and demonstrated several non-Newtonian behaviors, such as, the shear-thinning viscosity and the Fahraeus-Lindqvist effect [2–5]. In contrast, there have been relatively fewer studies which seek to connect the macroscopic rheology with the microhydrodynamics of individual erythrocytes.

Individual erythrocyte structurally resembles a sac of liquid (hemoglobin) enclosed by a lipid bilayer overlying a two-dimensional network of protein filaments [6,7]. At typical length scales of the cells, the bilayer-cytoskeleton complex can be modeled as a zero-thickness elastic membrane. Such simplified models of erythrocytes include capsules and vesicles which are viscous drops of an incompressible liquid surrounded by two-dimensional elastic membranes. The mechanical properties of the membrane are usually characterized by its resistance against shear deformation, surface-area dilatation, and formation of high curvature. Unlike a capsule, a vesicle membrane exhibits resistance against surface-area

dilatation and bending, and lacks any resistance against shear deformation.

When subject to a simple shear flow in a dilute suspension, erythrocytes, capsules, and vesicles may undergo a significant shape deformation while exhibiting primarily two types of motion: a tank-treading motion in which the particulate maintains an inclination angle with the flow direction while the interior liquid and the membrane make a continuous rotation, and a tumbling motion in which it flips like a rigid body [8–13]. These two types of motion can be predicted analytically by the Keller-Skalak (KS) theory [14]. For a shape-preserving ellipsoidal particulate made of a viscous internal fluid and an inextensible membrane, the tank-treading motion is predicted when the viscosity ratio ( $\lambda$ ) is less than a critical value  $\lambda_c$ , and the tumbling motion is predicted when  $\lambda > \lambda_c$ .

In addition to the tank-treading and tumbling motions, a swinging or oscillatory motion of red blood cells [12,15], nonspherical capsules [16–21], and vesicles [22–24] have recently been discovered. Recent studies have also shown a vacillating-breathing (or trembling) motion of the vesicles in the vicinity of the critical viscosity ratio  $\lambda_c$  at the onset of the transition from the tank treading to the tumbling motion [23–35]. The vacillating-breathing motion is characterized by a large periodic shape deformation accompanied by a large angular oscillation about a nearly zero-mean inclination angle. Similar vacillating-breathing motion has been predicted numerically for nonspherical capsules [21].

Studies that connect the bulk rheology with the microhydrodynamics of individual cell are relatively scarce. Following Batchelor's theory of suspension [36], Barthes-Biesel and Chhim [37] derived expressions of shear viscosity and

\*Corresponding author; [pbagchi@jove.rutgers.edu](mailto:pbagchi@jove.rutgers.edu)

normal stress differences of a dilute suspension of spherical capsules undergoing small deformation. The salient features of their result are: (i) the suspension exhibits a shear-thinning behavior; (ii) normal stress differences, to the leading order, depend linearly on shear rate  $\dot{\gamma}$  but independent of viscosity ratio  $\lambda$ . Using boundary integral simulations, Pozrikidis [38] and Ramanujan and Pozrikidis [17] computed dilute suspension rheology for spherical capsules undergoing large deformation. Pozrikidis [39] also briefly addressed time-dependent rheology of a dilute suspension of biconcave capsules.

For a dilute suspension of vesicles, a remarkable result is recently discovered by Misbah and co-workers [30,40,41]. In the limit of small excess area of the vesicles, they theoretically predict that the shear viscosity of the vesicle suspension first decreases reaching a minimum, and then increases with increasing  $\lambda$ . Thus the shear viscosity is higher when the vesicle is either in a pure tank-treading motion, or in a pure tumbling motion. The pronounced minimum of the shear viscosity (hereafter, referred to as *shear viscosity minimum*) occurs in the vicinity of the critical viscosity ratio  $\lambda_c$ , and hence, it is associated with the onset of the vacillating-breathing motion as the vesicle makes transition between the tank-treading and tumbling motions. This theoretical result is later supported by viscometric experiments using erythrocyte and vesicle suspensions [42].

In this paper we address the rheology of a dilute suspension of capsules. We focus exclusively on initially *spherical* capsules for which only a steady tank-treading motion is observed. Using three-dimensional numerical simulations of capsules in large deformation, we present a detailed and in-depth analysis of the suspension rheology over a broad range of viscosity ratio and shear rate for both strain-hardening and strain-softening membranes. In course of our analysis, we investigate (i) whether a shear viscosity minimum exists for the capsule suspension, similar to that found for a vesicle suspension as noted above [30,40–42], (ii) whether the shear viscosity minimum is a result of the onset of the vacillating-breathing mode, or it can occur even when the capsules are undergoing a steady tank-treading motion, and (iii) how the viscosity ratio of the interior and exterior fluids, and the elastic stresses on the capsule membrane individually contribute to the bulk rheology.

We find that a capsule suspension exhibits a shear viscosity minimum even when the capsules make a steady tank-treading motion. We then show that the viscosity minimum is a result of nontrivial contributions coming from the capsule membrane stresses and the viscosity ratio of the interior and suspending fluids.

## II. METHODOLOGY

Three-dimensional numerical simulations using front-tracking methods [43–46] are performed to simulate capsule dynamics and rheology. The numerical methodology has been described and validated in details in our previous publications [21,47,48] and briefly described here for the purpose of completeness. We consider an initially spherical capsule of radius  $a$  suspended in a linear shear flow  $\mathbf{u}^\infty$

$=\{\dot{\gamma}y, 0, 0\}$ . The liquids interior and exterior to the capsule are assumed to be incompressible and Newtonian with dynamic viscosities given by  $\lambda\mu_o$  and  $\mu_o$ , respectively, where  $\lambda$  is the viscosity ratio. The capsule membrane is assumed to be a thin two-dimensional (2D) elastic sheet having resistance against shear deformation, and area dilatation, but not bending. We consider both strain-hardening and strain-softening membranes. For the former, we use the strain energy function developed by Skalak *et al.* [49] (hereafter referred to as SK model),

$$W = \frac{E_s}{8}[(\epsilon_1^2 + \epsilon_2^2 - 2)^2 + 2(\epsilon_1^2 + \epsilon_2^2 - \epsilon_1^2\epsilon_2^2 - 1)] + \frac{E_a}{8}(\epsilon_1^2\epsilon_2^2 - 1)^2, \tag{1}$$

where  $\epsilon_1$  and  $\epsilon_2$  are the principal stretch ratios in the membrane and  $E_s$  and  $E_a$  are the moduli of shear deformation and area dilatation, respectively. For a strain-softening membrane, we use the neo-Hookean law (hereafter referred to as NH model),

$$W = \frac{E_s}{6}(\epsilon_1^2 + \epsilon_2^2 + \epsilon_1^{-2}\epsilon_2^{-2} - 3). \tag{2}$$

We scale all lengths by  $a$ , and time by  $1/\dot{\gamma}$ . The dimensionless time is denoted by  $t^* = t\dot{\gamma}$ . The three major dimensionless parameters are the capillary number  $\text{Ca} = \mu_o a \dot{\gamma} / E_s$ , the viscosity ratio  $\lambda$ , and the ratio of the area dilatation to shear deformation moduli  $C = E_a / E_s$ .

The fluid motion interior and exterior to the capsule is governed by the continuity and Navier-Stokes equations

$$\nabla \cdot \mathbf{u} = 0, \tag{3}$$

$$\rho \left[ \frac{\partial \mathbf{u}}{\partial t} + \mathbf{u} \cdot \nabla \mathbf{u} \right] = -\nabla p + \nabla \cdot \mu [\nabla \mathbf{u} + (\nabla \mathbf{u})^T], \tag{4}$$

where  $\mathbf{u}$  and  $p$  are the fluid velocity and pressure. The viscosity variation is expressed in terms of an indicator function  $I(\mathbf{x}, t)$  as

$$\mu(\mathbf{x}, t) = \mu_0 [1 + (\lambda - 1)I(\mathbf{x}, t)], \tag{5}$$

where  $I=1$  and  $0$ , in the interior and suspending fluids, respectively [43,44]. The entire flow domain, including the internal and suspending liquids, is discretized using a fixed (Eulerian) mesh, and the capsule surface is discretized using a moving (Lagrangian) mesh. Using the principle of virtual work, the elastic force  $\mathbf{f}$  generated in the membrane is computed from the strain energy function  $W$  as

$$\mathbf{f}(\mathbf{x}', t) = -\partial W / \partial \mathbf{v}, \tag{6}$$

where  $\mathbf{v}$  is the displacement of a Lagrangian point  $\mathbf{x}'$  on the capsule surface. The membrane stretching is coupled to the bulk flow by adding a source term  $\int_A \mathbf{f} \delta(\mathbf{x} - \mathbf{x}') d\mathbf{x}'$  to the Navier-Stokes equations where  $A$  implies capsule surface, and  $\delta$  is the three-dimensional Delta function [43–46]. The membrane is advected using the Lagrangian points whose velocity  $\mathbf{u}'$  is obtained by interpolating the fluid velocity from the surrounding Eulerian nodes using the Delta function as

$$\mathbf{u}'_A(\mathbf{x}', t) = \int_{\Omega} \mathbf{u}(\mathbf{x}, t) \delta(\mathbf{x} - \mathbf{x}') d\mathbf{x}, \quad (7)$$

where  $\Omega$  is the flow domain [43,44,47,48]. The viscosity  $\mu(\mathbf{x}, t)$  is updated by solving a Poisson equation for the indicator function  $I(\mathbf{x}, t)$  (see [44] for details). Note that the capsule is moved by moving the marker (Lagrangian) points on the surface. Once it is moved to a new position, the indicator function is computed to distribute the viscosity. Indeed one can use an advection equation for viscosity. But we find that over long time, viscosity advection introduces erroneous distribution and deviate from the exact location of the capsule.

The computation domain is a cube having lengths  $2\pi$  times the capsule radius. The flow is periodic in the  $x$  and  $z$  directions, and wall-bounded in the  $y$  direction. The Navier-Stokes equations are spatially discretized by a second-order finite difference scheme in  $x$  and  $y$ , and Fourier expansion in  $z$ , and temporally by a second-order time-split scheme. A velocity field that is not divergence free is first predicted using an advection-diffusion equation. Then a Poisson equation for pressure is solved. Using the new pressure, the predicted velocity is made divergence free. For details, see our previous publications [47,48]. Though the inertia terms are evaluated during time marching, the Reynolds number  $Re = \rho a^2 \dot{\gamma} / \mu_o \approx 10^{-2}$ , and hence, the effect of inertia is negligible. The singularity of the Delta function is avoided numerically by a smooth representation using cosine functions spanning over four Eulerian grids [43,44]. The flow domain is discretized using  $80^3$  Eulerian points, and the capsule surface is discretized using 5120 triangular elements.

The bulk stress of a dilute suspension, in dimensional form, is written as

$$\tilde{\Sigma}^{\text{bulk}} = \tilde{\Sigma}^{\infty} + \tilde{\Sigma}, \quad (8)$$

where  $\tilde{\Sigma}^{\infty} = 2\mu_o \mathbf{E}$  is the contribution due to the imposed linear flow  $\mathbf{u}^{\infty}$ ,  $\mathbf{E}$  is the strain-rate tensor, and  $\tilde{\Sigma}$  is the *particle stress tensor* that accounts for the contribution from the capsules [36]. The symbol  $\tilde{\phantom{x}}$  is used to indicate dimensional stress, whereas the dimensionless stress will be written without the symbol. For  $M$  number of identical capsules in a volume  $V$ , the particle stress tensor in dimensional form is given by

$$\tilde{\Sigma}_{ij} = \frac{1}{V} \sum_M \int_A [\sigma_{ik} n_k x'_j - \mu_o (u_i n_j + u_j n_i)] dA, \quad (9)$$

where  $\sigma_{ik}$  is the stress in the suspending fluid at the capsule membrane,  $\mathbf{n}$  is the unit vector normal to the capsule surface and directing outward,  $\mathbf{x}'$  and  $\mathbf{u}$  are the position and velocity on a capsule surface, and the integral is taken over the surface  $A$ . In the front-tracking method, we find it convenient to use an alternative expression for the dimensional particle stress tensor as

$$\tilde{\Sigma}_{ij} = \frac{1}{V} \sum_M \int_A [f_i x'_j + \mu_o (\lambda - 1) (u_i n_j + u_j n_i)] dA, \quad (10)$$

where  $\mathbf{f}$  is the elastic force in the membrane [17,38]. The particle stress tensor is made dimensionless by  $\mu_o \dot{\gamma} \phi$  where  $\phi$  is the capsule volume fraction. Then, the dimensionless particle stress tensor is given by

$$\Sigma_{ij} = \frac{\tilde{\Sigma}_{ij}}{\mu_o \dot{\gamma} \phi} = \frac{M}{V \mu_o \dot{\gamma} \phi} \int_A [f_i x'_j + \mu_o (\lambda - 1) (u_i n_j + u_j n_i)] dA. \quad (11)$$

All results are presented in this dimensionless form.

It is of interest to study the individual contributions of the membrane stress and viscosity ratio to the particle stress. Hence we introduce the *elastic* and *viscous* contributions in dimensionless form as

$$\Sigma_{ij}^{\text{el}} = \frac{M}{V \mu_o \dot{\gamma} \phi} \int_A f_i x'_j dA \quad (12)$$

and

$$\Sigma_{ij}^{\text{vis}} = \frac{M(\lambda - 1)}{V \dot{\gamma} \phi} \int_A (u_i n_j + u_j n_i) dA, \quad (13)$$

respectively, so that,

$$\Sigma_{ij} = \Sigma_{ij}^{\text{el}} + \Sigma_{ij}^{\text{vis}}. \quad (14)$$

The elastic contribution  $\Sigma^{\text{el}}$  arises due to the stresses developed in the capsule membrane, while the viscous contribution  $\Sigma^{\text{vis}}$  arises due to the viscosity ratio of the internal and suspending fluids.

Quantities of interest are the particle shear stress  $\Sigma_{xy}$ , the first normal stress difference  $N_1 = \Sigma_{xx} - \Sigma_{yy}$ , and the second normal stress difference  $N_2 = \Sigma_{yy} - \Sigma_{zz}$ , all expressed in dimensionless form. The dimensionless shear viscosity is related to the dimensional and dimensionless shear stresses as follows:

$$\frac{\mu_s}{\mu_o} = 1 + \frac{\tilde{\Sigma}_{xy}}{\mu_o \dot{\gamma}} = 1 + \phi \Sigma_{xy}. \quad (15)$$

Thus  $\Sigma_{xy}$  can be readily used to indicate the trends of the dimensionless shear viscosity (e.g., shear-thinning behavior, etc.). For the present simulations,  $\phi = 0.017$ .

### III. RESULTS

#### A. Capsule shape and orientation

We consider capsules of spherical resting shape for which only the *steady tank-treading* motion is observed. When placed in a shear flow, the capsule deforms and eventually attains a steady oblate shape, and aligns at a steady inclination angle with the flow direction. Figures 1(a) and 1(b) show the final capsule shape for  $\lambda=1$  and 13, both at  $Ca=0.6$ , for capsules with SK model ( $C=1$ ). Large deformation resulting to an elongated shape is observed at  $\lambda=1$ , whereas a nearly spherical shape is observed at  $\lambda=13$ . Figure 1(c)

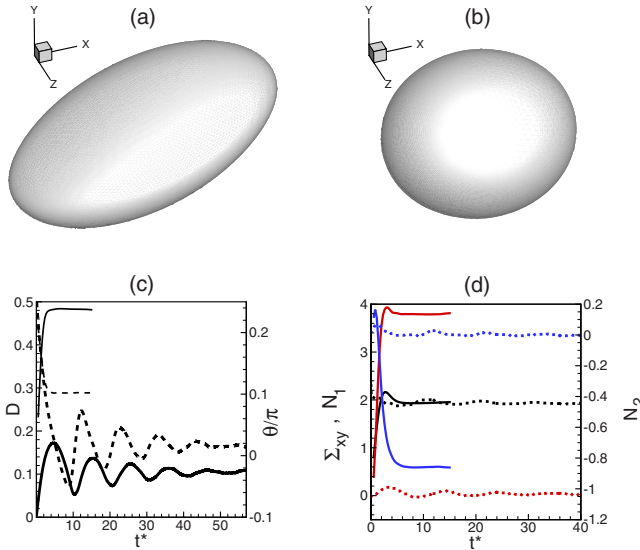


FIG. 1. (Color online) Sample results for spherical capsules with SK model ( $C=1$ ). (a) and (b) show the final shapes for  $Ca=0.6$ ,  $\lambda=1$  and  $Ca=0.6$ ,  $\lambda=13$ , respectively. (c) Time-dependent Taylor deformation parameter  $D$  (left axis, and continuous lines) and inclination angle  $\theta$  (right axis, and dash lines) for two cases:  $Ca=0.6$ ,  $\lambda=1$  (thin lines), and  $Ca=0.6$ ,  $\lambda=13$  (thick lines). (d) Time-dependent particle stress components  $\Sigma_{xy}$  (black lines, left axis),  $N_1$  (red lines, left axis), and  $N_2$  (blue lines, right axis) for two cases:  $Ca=0.6$ ,  $\lambda=1$  (continuous lines), and  $Ca=0.6$ ,  $\lambda=13$  (dotted lines). Here  $t^* = t\dot{\gamma}$  is the dimensionless time.

shows the time evolution of the Taylor deformation parameter  $D = (L - B) / (L + B)$  where  $L$  and  $B$  are the semimajor and minor axes of the deformed capsule in the shear plane. Also shown is the inclination angle  $\theta$  that the major axis makes with the flow direction ( $x$  axis). The inclination angle decreases with increasing  $\lambda$ . We also note that the  $\lambda=1$  case quickly reaches the steady state, whereas the  $\lambda=13$  case exhibits damped oscillations before reaching a steady state. Damped oscillations are typically observed for higher values of  $Ca$  and  $\lambda$ . Simulations are run for longer times [as shown in Fig. 1(c)] to ensure that such oscillations become negligible. Time evolution of  $\Sigma_{xy}$ ,  $N_1$ , and  $N_2$  are presented in Fig. 1(d) showing that they also reach steady values.

The oscillations observed in Fig. 1(c) were also reported in earlier numerical studies (e.g., [17]) using different numerical methods. Given the very few experimental studies on capsules relevant to the present work, we cannot make a definite conclusion whether these oscillations are numerical or physical. It would require further study that is beyond the scope of this paper.

Steady-state values of  $D$  and  $\theta$  as functions of  $Ca$  for various  $\lambda$  are shown in Fig. 2 for SK model ( $C=1$ ). These results agree well with previously published data [15,50,51]. For more details on validations against previous numerical works, experimental works, and small-deformation theory, see our earlier publications [47,48]. Qualitative trends of  $D$  and  $\theta$  should be borne in mind as they will be used later to explain the trends of the rheology. Figure 2 shows that capsule deformation increases and the inclination angle decreases with increasing  $Ca$ . In contrast, both deformation and inclination angle decrease with increasing  $\lambda$ .

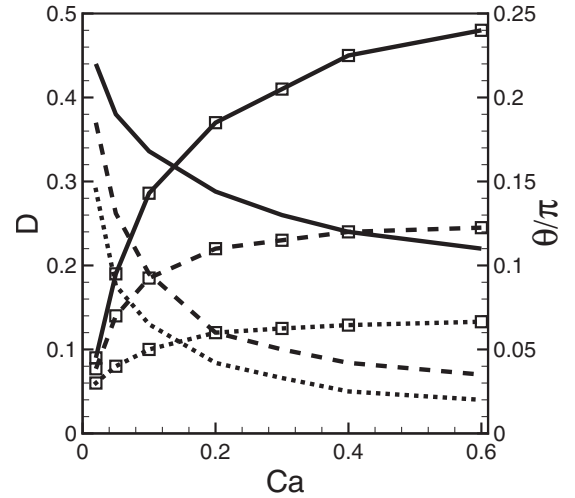


FIG. 2. Steady-state values of the Taylor deformation parameter  $D$  (left axis, and lines with symbols) and the inclination angle  $\theta$  (right axis, and lines without symbols) for capsules with SK model ( $C=1$ ).  $\lambda=1$  (continuous lines), 5 (dash lines), and 10 (dotted lines).

## B. Shear stress

We now come to the main focus of this article, which is the particle shear stress  $\Sigma_{xy}$ . The SK model with  $C=1$  is considered in Fig. 3. The variation in  $\Sigma_{xy}$  with  $Ca$  presented in Fig. 3(a) shows that  $\Sigma_{xy}$  decreases with increasing  $Ca$ . Hence, the capsule suspension exhibits a shear-thinning behavior.

The effect of  $\lambda$  is shown in Fig. 3(b). Two different trends are observed at low and high values of  $Ca$ . Consider first the low values of  $Ca$  in the range  $Ca \leq 0.1$ . In this range  $\Sigma_{xy}$  decreases uniformly with increasing  $\lambda$ . This result is counterintuitive as capsule deformation is known to decrease with increasing  $\lambda$  (Fig. 2), and a reduced deformation should result an increased  $\Sigma_{xy}$ . This result suggests that the trend of  $\Sigma_{xy}$  cannot be explained by capsule geometry alone.

The above result of decreasing  $\Sigma_{xy}$  with increasing  $\lambda$  is also in contradiction to that of a dilute emulsion of liquid drops with constant interfacial tension [52]. For a liquid drop emulsion, in the limit of small deformation, we have

$$\Sigma_{xy} = \frac{1 + 5\lambda/2}{1 + \lambda}, \quad (16)$$

which gives an increasing  $\Sigma_{xy}$  with increasing  $\lambda$ , unlike the computed results for capsules. We however note that the small-deformation theory of capsule suspension does predict a (linear) decrease in  $\Sigma_{xy}$  with increasing  $\lambda$  [37]. A similar trend is also predicted for emulsions of surfactant-covered liquid drops [53].

Consider now the trends of  $\Sigma_{xy}$  versus  $\lambda$  at higher shear rates [ $Ca > 0.1$ , Fig. 3(b)]. We see a remarkably nonintuitive result:  $\Sigma_{xy}$  first decreases reaching a minimum, and then increases with increasing  $\lambda$ .

Hence, the capsule suspension exhibits a shear viscosity minimum at moderate values of viscosity ratio, and at high shear rates. In this respect, there is some qualitative similar-

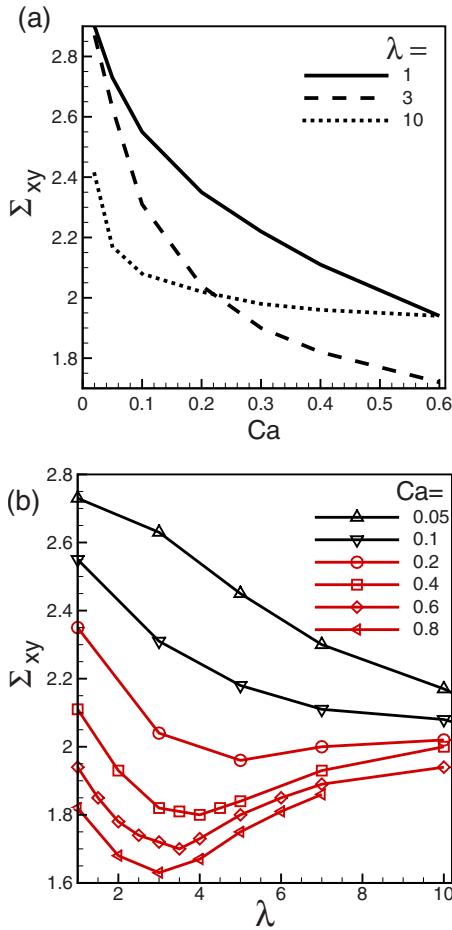


FIG. 3. (Color online) Particle shear stress  $\Sigma_{xy}$  in dimensionless form for capsules with SK model ( $C=1$ ). (a) Effect of  $Ca$  at constant  $\lambda$ , and (b) effect of  $\lambda$  at constant  $Ca$ .

ity between the present results and those for vesicle suspension as predicted and observed by Misbah and co-workers [30,40–42]. However, since the capsules in our simulations are in a steady tank-treading motion, the physical mechanisms underlying the shear viscosity minimum are completely different, as will be shown later.

We note again that the shear viscosity minimum cannot be explained based on the capsule shape alone, as  $D$  and  $\theta$  both decrease continually with increasing  $\lambda$  (Fig. 2). This anomalous behavior was not predicted by the small-deformation theory of suspension of capsules or surfactant-covered drops [37,53].

We now show that the shear viscosity minimum exists for strain-softening membranes as well by considering capsules with the NH model in Fig. 4. As before, the salient features of Fig. 4 are: (i) a shear-thinning behavior with respect to  $Ca$ , (ii) a uniform decrease in  $\Sigma_{xy}$  with increasing  $\lambda$  at low shear rates ( $Ca \leq 0.05$ ), and (iii) an initial decrease in  $\Sigma_{xy}$  reaching a minimum, followed by an increase with  $\lambda$  at high shear rates ( $Ca > 0.1$ ).

The nontrivial behavior of  $\Sigma_{xy}$  suggest that the bulk rheology is dictated not only by the capsule geometry (deformation and inclination) but also by the contributions coming from the membrane stress and viscosity ratio. Hence, we look at the elastic component  $\Sigma_{xy}^{el}$  and the viscous component

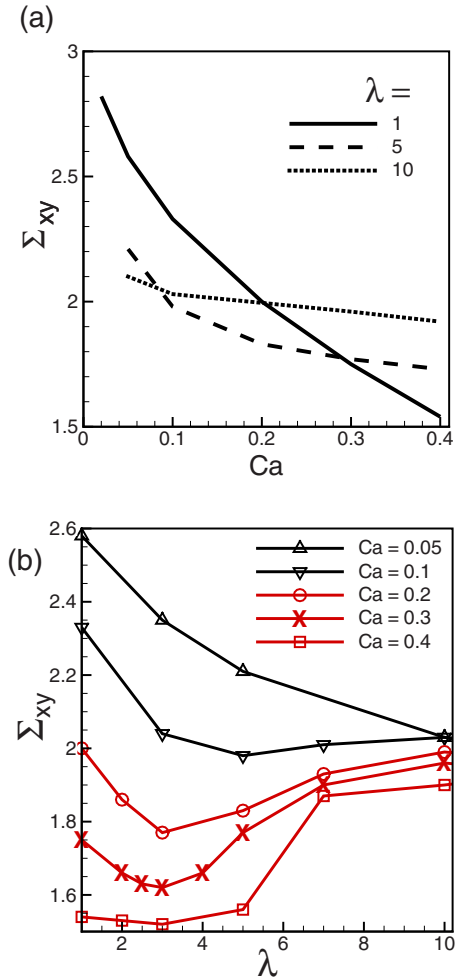


FIG. 4. (Color online) Particle shear stress  $\Sigma_{xy}$  in dimensionless form for capsules with NH model. (a) Effect of  $Ca$  at constant  $\lambda$ , and (b) effect of  $\lambda$  at  $Ca$ .

$\Sigma_{xy}^{vis}$  in Fig. 5 as functions of  $Ca$ . First, in Fig. 5(a) we see that  $\Sigma_{xy}^{el}$  decreases with increasing  $Ca$ . Thus the elastic component is shear thinning in nature. This result is nonintuitive as an increased membrane tension at higher  $Ca$  should result increasing  $\Sigma_{xy}^{el}$  as one would expect from the definition in Eq. (12). The second observation in Fig. 5(b) is that the viscous component  $\Sigma_{xy}^{vis}$  increases with increasing  $Ca$ . Hence, the vis-

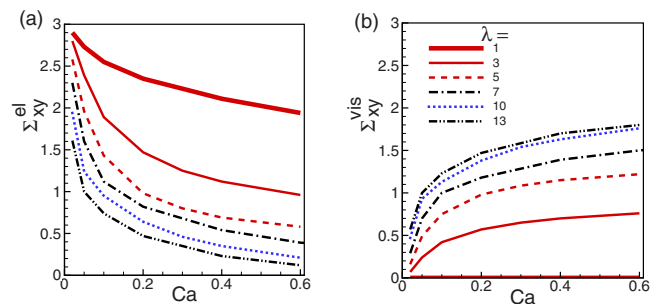


FIG. 5. (Color online) Elastic ( $\Sigma_{xy}^{el}$ ) and viscous ( $\Sigma_{xy}^{vis}$ ) components in dimensionless form with varying  $Ca$  for different values of  $\lambda$  for SK model with  $C=1$ . Symbols have same meanings in (a) and (b).

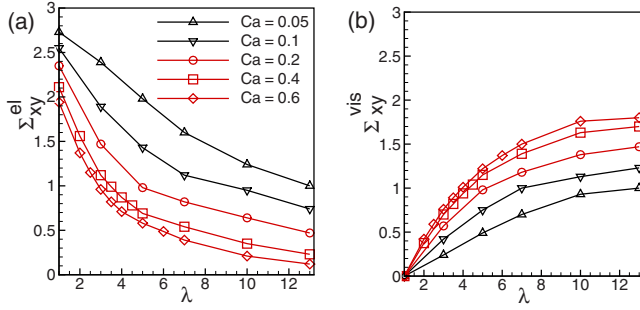


FIG. 6. (Color online) Elastic ( $\Sigma_{xy}^{\text{el}}$ ) and viscous ( $\Sigma_{xy}^{\text{vis}}$ ) components in dimensionless form with varying  $\lambda$  for different Ca for SK model with  $C=1$ . Symbols have same meanings in (a) and (b).

ous contribution is shear-thickening. This trend is also unexpected as Eq. (13) suggests that  $\Sigma_{xy}^{\text{vis}}$  should be independent of Ca.

To explore the origin of the shear viscosity minimum, we plot  $\Sigma_{xy}^{\text{el}}$  and  $\Sigma_{xy}^{\text{vis}}$  versus  $\lambda$  in Fig. 6. Surprisingly, we find that the elastic contribution decreases with increasing  $\lambda$ . As will be seen later, this decrease is due to a reduction in the membrane stresses. In contrast, the viscous contribution increases with increasing  $\lambda$ . This result can be used to explain the two different trends of  $\Sigma_{xy}$  at low and high values of Ca. At low Ca,  $\Sigma_{xy}^{\text{el}} > \Sigma_{xy}^{\text{vis}}$ , and, hence, the total shear stress  $\Sigma_{xy}$  follows the trend of the elastic component  $\Sigma_{xy}^{\text{el}}$ , and decreases with increasing  $\lambda$ . At higher Ca,  $\Sigma_{xy}^{\text{el}} > \Sigma_{xy}^{\text{vis}}$  for smaller values of  $\lambda$ , but  $\Sigma_{xy}^{\text{el}} < \Sigma_{xy}^{\text{vis}}$  for larger values of  $\lambda$ . Thus,  $\Sigma_{xy}$  follows the trend of  $\Sigma_{xy}^{\text{el}}$  for smaller values of  $\lambda$ , but it follows the trend of  $\Sigma_{xy}^{\text{vis}}$  for higher values of  $\lambda$ . And, hence,  $\Sigma_{xy}$  exhibits a minimum at the intermediate values of  $\lambda$  resulting the shear viscosity minimum. This analysis clearly shows that the opposite trends in  $\Sigma_{xy}^{\text{el}}$  and  $\Sigma_{xy}^{\text{vis}}$  are responsible for the shear viscosity minimum in capsule suspension.

We now seek to explain the trends of the elastic and viscous components. The elastic component  $\Sigma_{xy}^{\text{el}}$  can be further decomposed in to two contributions. The first one depends on capsule shape and alignment alone and can be written as

$$\Sigma^{\text{el,iso}} = -\Gamma \int_A \left( \mathbf{nn} - \frac{\mathbf{I}}{3} \right) dA, \quad (17)$$

where the constant  $\Gamma$  represents an isotropic membrane tension. The second contribution arises from the anisotropic distribution of the membrane tension. For a liquid drop with a constant surface tension,  $\Gamma$  becomes the surface tension, and the anisotropic part vanishes. Then,  $\Sigma^{\text{el}} = \Sigma^{\text{el,iso}}$  which depends only on the drop shape and alignment. For a capsule, the anisotropic contribution is nonzero. We seek to address if the above isotropic model can qualitatively explain the trends of  $\Sigma_{xy}^{\text{el}}$  as observed in Figs. 5 and 6.

Figure 7 shows  $\Sigma_{xy}^{\text{el,iso}}$  evaluated using Eq. (17) for oblate spheroids of aspect ratio (semimajor to minor axes)  $\alpha=1$ , 1.25, and 1.67, as a function of the inclination angle  $\theta$ . The results are shown in arbitrary units, and taking  $\Gamma=1$ . For the stationary capsule dynamics, only  $0 \leq \theta \leq \pi/4$  is of interest. We see that  $\Sigma_{xy}^{\text{el,iso}}=0$  for  $\alpha=1$  at any inclination angle, as expected from Eq. (17). For  $\alpha \neq 1$ ,  $\Sigma_{xy}^{\text{el,iso}}$  is maximum at  $\theta = \pi/4$ , and it decreases with decreasing  $\theta$  and  $\alpha$ . This result can completely explain the qualitative trends of  $\Sigma_{xy}^{\text{el}}$  by recalling from Fig. 2 that  $\theta$  decreases with increasing Ca and  $\lambda$ , and  $D$  decreases with increasing  $\lambda$ . Thus,  $\Sigma_{xy}^{\text{el,iso}}$  should decrease with increasing Ca and  $\lambda$ . Thus, the qualitative trend of  $\Sigma_{xy}^{\text{el}}$  follows that of  $\Sigma_{xy}^{\text{el,iso}}$ .

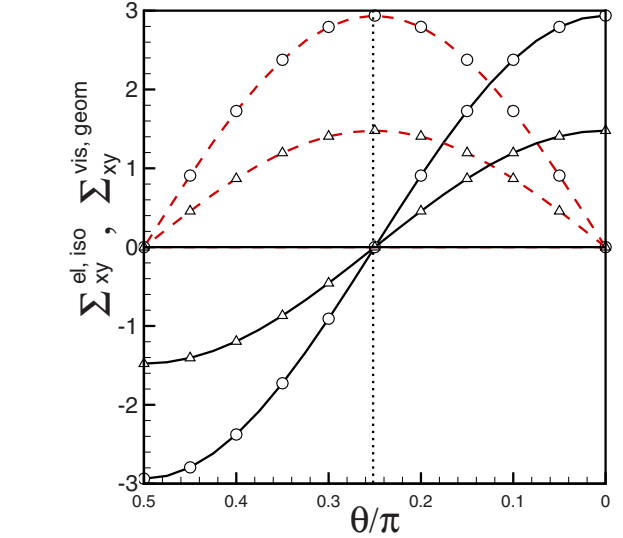


FIG. 7. (Color online) Variation of  $\Sigma_{xy}^{\text{el,iso}}$  (dash red lines), and  $\Sigma_{xy}^{\text{vis,geom}}$  (continuous black lines) as functions of inclination angle  $\theta$  for shape-preserving oblate spheroids for aspect ratios 1 (no symbol), 1.25 (triangles), and 1.67 (circles).

Now we analyze the qualitative trends of the viscous contributions  $\Sigma_{xy}^{\text{vis}}$ . At steady-state, the shape of the capsule and its alignment with the flow direction are fixed (for the unstressed spherical shape considered here) while the capsule membrane undergoes the tank-treading motion. Then the membrane velocity can be expressed as  $\mathbf{u}(\mathbf{x}', t) = |\mathbf{u}(\mathbf{x}', t)| \mathbf{t}$ , where  $\mathbf{t}$  is tangent to the capsule surface on the shear plane. Approximating  $|\mathbf{u}|$  by  $a/T$  where  $T$  is the tank-treading period, we write from Eq. (13)

$$\Sigma^{\text{vis}} \approx \frac{aM(\lambda-1)}{TV\dot{\gamma}\phi} \int_A (\mathbf{tn} + \mathbf{nt}) dA. \quad (18)$$

Then, we introduce  $\Sigma^{\text{vis,geom}}$  as

$$\Sigma^{\text{vis,geom}} = \Gamma \int_A (\mathbf{tn} + \mathbf{nt}) dA, \quad (19)$$

which is the viscous contribution modeled based on the capsule geometry, and neglecting the effect of  $T$ . Here  $\Gamma$  is arbitrary. The integral in Eq. (19) is used to illustrate the trends of  $\Sigma_{xy}^{\text{vis}}$ . For this purpose,  $\Sigma_{xy}^{\text{vis,geom}}$  is evaluated using Eq. (19) for oblate spheroids for aspect ratios  $\alpha=1$ , 1.25, and 1.67, and plotted in Fig. 7 as a function of  $\theta$ . We see that  $\Sigma_{xy}^{\text{vis,geom}}=0$  for  $\alpha=1$ , as expected. For  $\alpha > 1$ ,  $\Sigma_{xy}^{\text{vis,geom}}$  is minimum at  $\theta = \pi/4$ , and it increases with decreasing  $\theta$  and increasing  $\alpha$ . Recalling from Fig. 2 that deformation increases and  $\theta$  decreases with increasing Ca, we see that the trend of  $\Sigma_{xy}^{\text{vis,geom}}$  can explain the trends of  $\Sigma_{xy}^{\text{vis}}$  versus Ca. Recalling further from Fig. 2 that inclination  $\theta$  decrease with

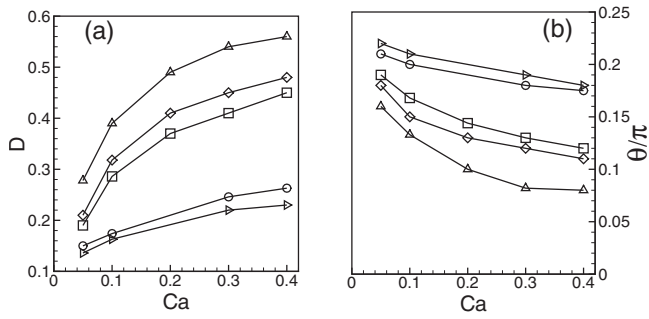


FIG. 8. Effect of area dilatation on (a) capsule deformation and (b) inclination angle. Symbols represent NH model ( $\Delta$ ), and SK models with  $C=0.1$  ( $\diamond$ ), 1 ( $\square$ ), 50 ( $\circ$ ), and 100 ( $\triangleright$ ). Here  $\lambda=1$ .

increasing  $\lambda$ , we see again that  $\Sigma_{xy}^{vis,geom}$  can also explain the trend of  $\Sigma_{xy}^{vis}$  versus  $\lambda$ .

**C. Effect of area dilatation**

Next we consider the effect of capsule surface-area dilatation. Figure 8 shows the steady-state deformation parameter  $D$  and inclination angle  $\theta$  as functions of  $Ca$  for five cases: the NH model, and the SK model with  $C=0.1, 1, 50,$  and  $100$ . The viscosity ratio is fixed at  $\lambda=1$ . For all cases,  $D$  increases and  $\theta$  decreases with increasing  $Ca$ . In contrast, increasing the values of  $C$  results in reduced deformation and higher inclination angle. Reduced deformation at higher values of  $C$  is achieved via reduced surface area dilatation. The area dilatation is maximum for the neo-Hookean membrane for which the area increases by 4.5% and 29% of the initial area for  $Ca=0.05$  and  $0.4$ , respectively. For the SK model at  $C=1$ , the area increases by 1.5% and 14.1% for  $Ca=0.05$  and  $0.4$ , respectively. At  $C=100$ , the respective area increases are only 0.16% and 1.8%.

The effect of area dilatation on  $\Sigma_{xy}$  is shown in Fig. 9 by considering four cases: the NH model, and the SK model with  $C=0.1, 1,$  and  $50$ . The shear-thinning behavior is prominent for the NH model, and for SK model at high area dilatation (i.e., low to moderate values of  $C$ ). At  $C \geq 50$ , the shear-thinning behavior is nearly absent due to a reduced capsule deformation.

Increasing the values of  $C$  also results in increasing values of  $\Sigma_{xy}$ . This can be understood based on the reduction in capsule deformation with increasing  $C$  as observed in Fig. 8.

For the SK model with  $C=0.1$  and  $1$ ,  $\Sigma_{xy}$  first reaches a minimum, and then increases with increasing  $\lambda$ . For  $C \geq 50$ ,  $\Sigma_{xy}$  is observed to decrease continually with increasing  $\lambda$ . Thus, for a capsule suspension, the shear viscosity minimum is observed for area-dilating membranes but not for nearly incompressible membranes.

The absence of a shear viscosity minimum for the nearly incompressible membranes can be understood again by decomposing the shear stress  $\Sigma_{xy}$  in to its elastic and viscous components. Figure 10 shows that at a fixed value of  $\lambda$ , the elastic component is the lowest for the NH model, and it increases with increasing  $C$  for the SK model. In contrast, the viscous component is the maximum for the NH model, and it decreases with increasing  $C$  for the SK model. For

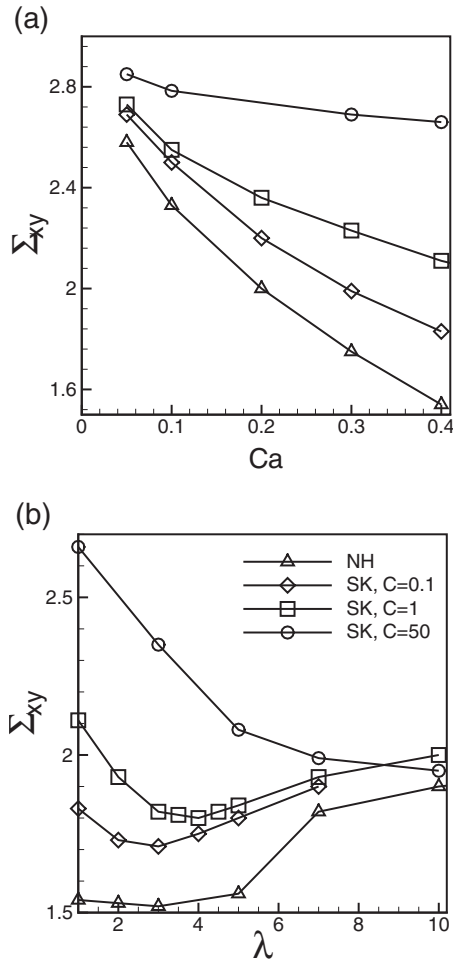


FIG. 9. Effect of area dilatation on  $\Sigma_{xy}$ . (a) Variation with respect to  $Ca$  at  $\lambda=1$  and (b) variation with respect to  $\lambda$  at  $Ca=0.4$ . Symbols represent NH model ( $\Delta$ ), and SK models with  $C=0.1$  ( $\diamond$ ), 1 ( $\square$ ), and 50 ( $\circ$ ).

$C \geq 50$ , the elastic component is mostly greater than the viscous component over the range of  $\lambda$ . Since the elastic component decreases continually with increasing  $\lambda$ , the shear viscosity minimum is not observed for nearly incompressible membranes.

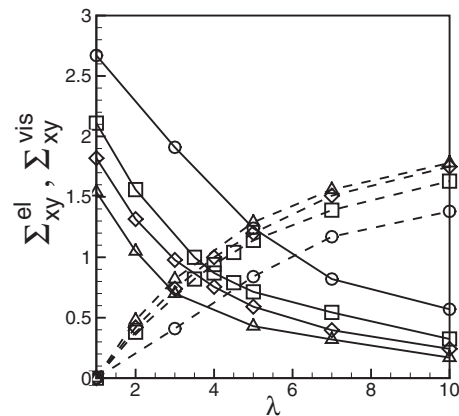


FIG. 10. Effect of area dilatation on  $\Sigma_{xy}^{el}$  (continuous lines) and  $\Sigma_{xy}^{vis}$  (dash lines). Symbols represent NH model ( $\Delta$ ), and SK models with  $C=0.1$  ( $\diamond$ ), 1 ( $\square$ ), and 50 ( $\circ$ ). Here  $Ca=0.4$ .

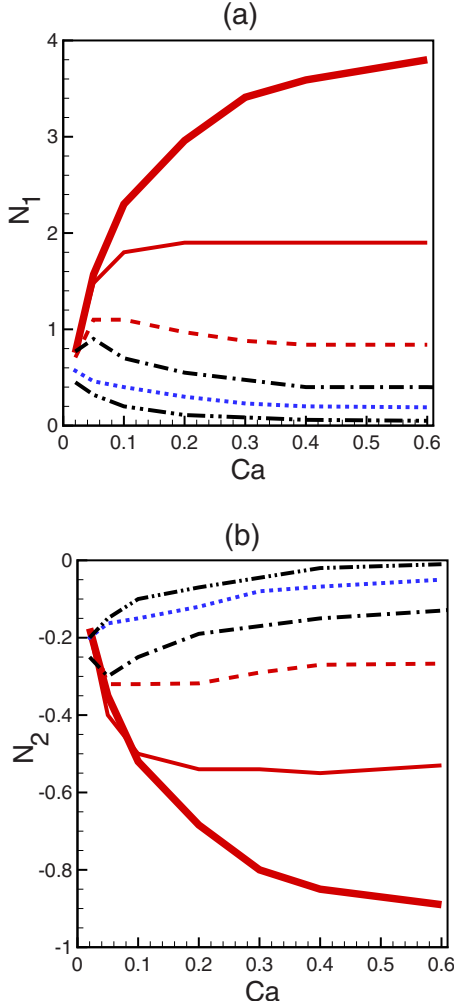


FIG. 11. (Color online)  $N_1$  and  $N_2$  for capsules with SK model ( $C=1$ ).  $\lambda=1$  (thick red lines), 3 (thin red lines), 5 (dash red lines), 7 (black dash-dot lines), 10 (blue dotted lines), and 13 (black dash-dot-dot lines).

For the SK model, the membrane stresses develop due to both area dilatation and shear deformation. Thus, one can write  $\Sigma_{xy}^{el} = \Sigma_{xy}^{sh} + \Sigma_{xy}^{di}$  where  $\Sigma_{xy}^{sh}$  represents the contribution from the shear elasticity  $E_s$ , and  $\Sigma_{xy}^{di}$  represents the contribution from the area-dilatation modulus  $E_a$ . We find that  $\Sigma_{xy}^{sh}$  is shear thinning, but  $\Sigma_{xy}^{di}$  is shear thickening. For  $C \geq 50$  at high capillary numbers,  $\Sigma_{xy}^{di}$  exceeds  $\Sigma_{xy}^{sh}$  by several factors. Hence, for nearly incompressible membranes, the bulk rheology is chiefly dictated by  $E_a$ .

#### D. Normal stress differences

The normal stress differences  $N_1$  and  $N_2$  for capsules with the SK model are shown in Fig. 11. Positive values of  $N_1$  and negative values of  $N_2$ , with  $|N_2| < N_1$ , are observed for all cases, as typical of emulsions. The dependence of the normal stress differences on  $Ca$  and  $\lambda$  is counterintuitive. At  $\lambda=1$ , both  $N_1$  and  $|N_2|$  increase with increasing  $Ca$  indicating an increasing elastic nature of the emulsion. At  $\lambda=3$ ,  $N_1$  and  $|N_2|$  first increase with increasing  $Ca$ , but attain constant values at higher shear rates. For  $\lambda=5$  and 7,  $N_1$  and  $|N_2|$  first

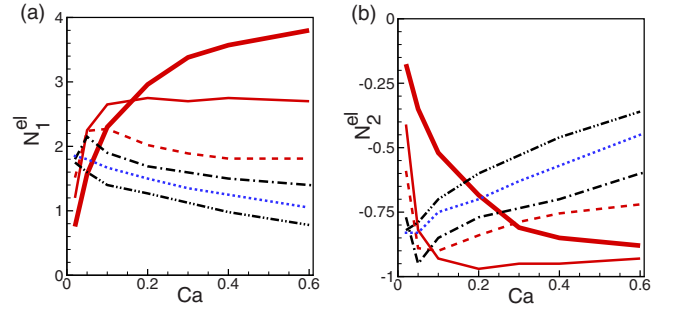


FIG. 12. (Color online) Effect of  $Ca$  on the elastic contributions (a)  $N_1^{el}$ , and (b)  $N_2^{el}$  for SK model with  $C=1$ . Line patterns represent different values of  $\lambda$  as in Fig. 11.  $\lambda=1$  (thick red lines), 3 (thin red lines), 5 (dash red lines), 7 (black dash-dot lines), 10 (blue dotted lines), and 13 (black dash-dot-dot lines).

increase to maximum values, but then decrease with increasing  $Ca$ . For  $\lambda=10$ , and 13,  $N_1$  and  $|N_2|$  monotonically decrease with increasing  $Ca$ , thus completely reversing the trend seen at  $\lambda=1$ .

It is worth mentioning that the trends of computed  $N_1$  and  $N_2$  as observed in Fig. 11 are completely different from those predicted by the small-deformation theories. As mentioned before, the second-order theory of capsule deformation, and the third-order theory for surfactant-covered liquid drops predict that  $N_1$  and  $N_2$  depend linearly on  $Ca$  but independent of  $\lambda$  [37,53]. In contrast, the computed values show a non-linear dependence on  $Ca$  and  $\lambda$ .

It is also worth noting the differences with the theoretical results for vesicle suspension. Similar to  $\Sigma_{xy}$ , the theoretical analysis for vesicle suspension predicts that  $N_1$  first reaches a minimum and then increases with increasing values of  $\lambda$  [41]. In contrast, for a capsule suspension, our computations show that  $N_1$  and  $|N_2|$  decrease almost monotonically with increasing  $\lambda$ .

We note that in viscometric experiments, the shear rate is readily available, and the results are presented for  $\tilde{N}_1/\dot{\gamma}^2$ . Since the computations performed, and the input parameters provided, are in dimensionless form, presenting the results in terms of  $N_1$  and  $N_2$  as defined in Sec. II is justified. We also note that  $N_1$  and  $N_2$  approach zero as  $Ca$  (or,  $\dot{\gamma}$ ) goes to zero (hard sphere limit). Further, in agreement with polymer suspensions, we see that  $N_2 < 0$ , and much smaller than  $N_1$ .

We now explain the trends of  $N_1$  and  $N_2$  by looking at the viscous and elastic components. We recall from Eq. (14) that

$$N_1 = N_1^{el} + N_1^{vis} \quad (20)$$

and

$$N_2 = N_2^{el} + N_2^{vis}. \quad (21)$$

The elastic components  $N_1^{el}$  and  $N_2^{el}$  with  $Ca$  are shown in Fig. 12. We see that  $N_1^{el}$  is positive and larger than  $N_1$ , whereas  $N_2^{el}$  is negative, and its magnitude is larger than  $|N_2|$ . This is because, as will be seen later, the viscous component  $N_1^{vis}$  is negative, and  $N_2^{vis}$  is positive. We also note that for  $\lambda=1$ ,  $N_1^{el} = N_1$  and  $N_2^{el} = N_2$  since the viscous component is absent and that  $N_1^{el}$  and  $|N_2^{el}|$  increase with increasing  $Ca$  following

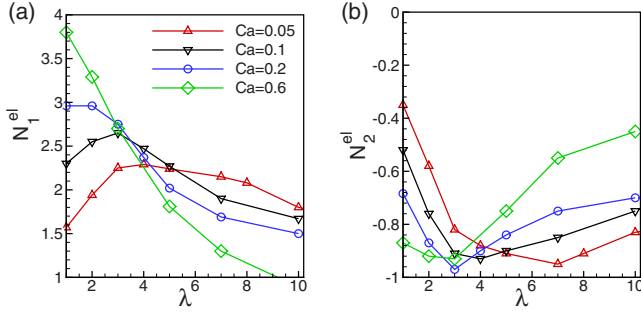


FIG. 13. (Color online) Effect of  $\lambda$  on the elastic contributions (a)  $N_1^{el}$ , and (b)  $N_2^{el}$  for SK model with  $C=1$ . Line patterns represent different values of  $Ca$  as indicated.

the trends of  $N_1$  and  $|N_2|$ . For  $\lambda > 1$ , however, a remarkably different behavior is observed. For  $\lambda=3$ ,  $N_1^{el}$  and  $|N_2^{el}|$  rapidly increase but then become independent of  $Ca$ . For  $\lambda \geq 5$ ,  $N_1^{el}$  and  $|N_2^{el}|$  first increase to a maximum, but then decrease with increasing  $Ca$ . This trend is completely different from that observed at  $\lambda=1$ . This behavior implies that at high viscosity ratio, the elastic nature of the suspension diminishes with increasing shear rates. Thus, the capsule suspension exhibits elastic normal stress maximums at moderate viscosity ratio and shear rate.

The anomalous trends of  $N_1^{el}$  and  $N_2^{el}$  are further explored in Fig. 13 where they are plotted with respect to  $\lambda$ . The figure clearly shows that at smaller values of  $\lambda$ , the magnitudes of the elastic components increase with increasing  $Ca$ , while the trend is reversed at larger values. For  $Ca=0.05$  and  $0.1$ ,  $N_1^{el}$  and  $|N_2^{el}|$  first increase, and then decrease with increasing  $\lambda$ . For  $Ca \geq 0.6$ ,  $N_1^{el}$  and  $|N_2^{el}|$  continually decrease with increasing  $\lambda$ .

We now investigate if the complex trends of  $N_1^{el}$  and  $N_2^{el}$  can be predicted by the isotropic model given by Eq. (17), which accounts for capsule geometry only. Figure 14 shows  $N_1^{el,iso}$  and  $N_2^{el,iso}$  computed using Eq. (17) for oblate spheroids of aspect ratio  $\alpha=1$ , 1.25, and 1.67, with varying  $\theta$ . The results are shown in arbitrary units taking  $\Gamma=1$ . For  $\alpha$

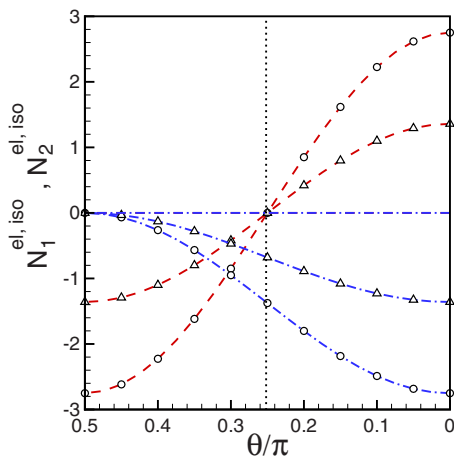


FIG. 14. (Color online) Variation in  $N_1^{el,iso}$  (red dash lines) and  $N_2^{el,iso}$  (blue dash-dot lines) as functions of inclination angle  $\theta$  for shape-preserving oblate spheroids for aspect ratios 1 (no symbol), 1.25 (triangles), and 1.67 (circles).

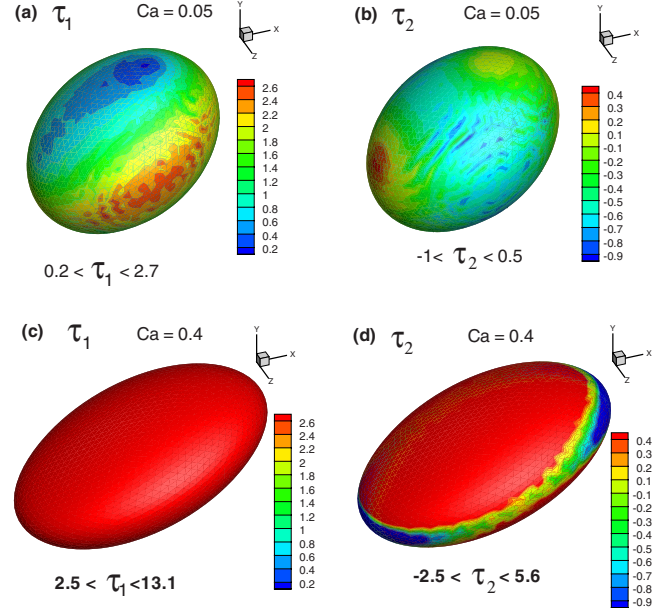


FIG. 15. (Color online) Distribution of the principal membrane tensions  $\tau_1$  and  $\tau_2$  for  $\lambda=1$  for two capillary numbers [(a) and (b)] 0.05 and [(c) and (d)] 0.4. The color changes from red to blue as the value decreases. The contour ranges are indicated for each case. (SK model with  $C=1$ ).

$=1$ , we see that  $N_1^{el,iso}=N_2^{el,iso}=0$  at any  $\theta$ , as expected. For  $\alpha > 1$ ,  $N_1^{el,iso}$ , and  $|N_2^{el,iso}|$  increase with increasing  $\alpha$  and decreasing  $\theta$ . This trend is the same that was observed for  $N_1^{el}$  and  $N_2^{el}$  for  $\lambda=1$ , but not for  $\lambda > 1$  (Figs. 12 and 13). Thus, the isotropic model fails to explain the trends of  $N_1^{el}$  and  $N_2^{el}$  for  $\lambda > 1$ .

For  $\lambda > 1$ , it appears that the anisotropy of the membrane tension contributes significantly to the elastic components. This can be illustrated by looking at the distribution of the membrane principal tensions

$$\tau_1 = \frac{1}{\epsilon_2} \frac{\partial W}{\partial \epsilon_1}, \quad \tau_2 = \frac{1}{\epsilon_1} \frac{\partial W}{\partial \epsilon_2}. \quad (22)$$

Figures 15 and 16 show the contours of  $\tau_1$  and  $\tau_2$  for  $\lambda=1$  and 7, respectively, for two capillary numbers, 0.05 and 0.4. Consider first the  $\lambda=1$  case (Fig. 15). We see that  $\tau_1$  is always positive, but  $\tau_2$  can be negative (which is indicative of a compressive stress). At  $Ca=0.05$ ,  $\tau_2 < 0$  over a large area. As  $Ca$  is increased from 0.05 to 0.4, we see that the magnitudes of  $\tau_1$  and  $\tau_2$  increase significantly, and that  $\tau_2 > 0$  over a large area. Thus, the area-integrated effect of the membrane tensions is to increase the magnitudes of  $N_1^{el}$  and  $N_2^{el}$  with increasing  $Ca$  as observed in Fig. 12 for  $\lambda=1$ .

Consider now the  $\lambda=7$  case (Fig. 16). At  $Ca=0.05$ , the contours of  $\tau_1$  and  $\tau_2$  are similar to those obtained at  $\lambda=1$ . But at  $Ca=0.4$ , we see that  $\tau_1$  has become negative, and  $\tau_2$  is dominantly negative. The integrated effect of such negative membrane tensions is to reduce the values of  $N_1^{el}$  and  $|N_2^{el}|$ . Hence,  $N_1^{el}$  and  $N_2^{el}$ , unlike  $N_1^{el,iso}$  and  $N_2^{el,iso}$ , exhibit non-monotonic trends with respect to  $Ca$  and  $\lambda$  due to the non-monotonic trends of the membrane tensions.

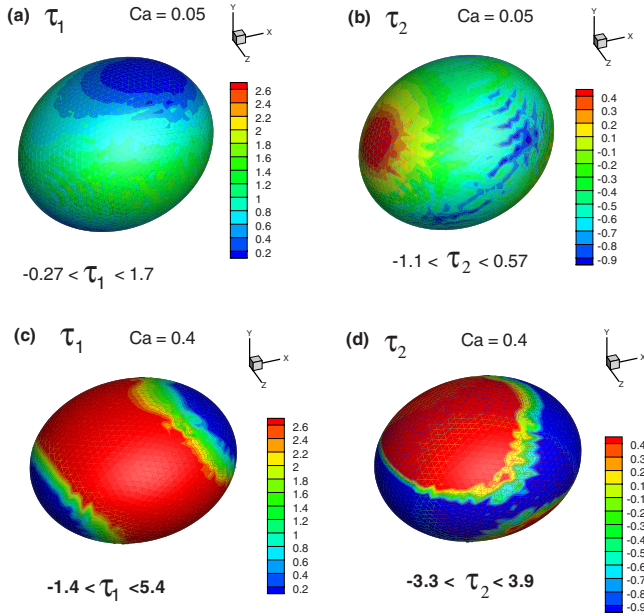


FIG. 16. (Color online) Same as in Fig. 15 but for  $\lambda=7$ .

The viscous components of the normal stress differences,  $N_1^{vis}$  and  $N_2^{vis}$ , are shown in Fig. 17. The viscous components have opposite signs than their elastic counterparts;  $N_1^{vis}$  is negative, and  $N_2^{vis}$  is positive. Figures 17(a) and 17(b) illustrate the Ca-dependence of  $N_1^{vis}$  and  $N_2^{vis}$ . Interesting behavior is noted when variations with respect to Ca at  $\lambda \geq 5$  are considered. In this range,  $|N_1^{vis}|$  and  $N_2^{vis}$  first increase reaching maximum values, and then decrease with increasing Ca. This nonmonotonic trend is quite different from that observed for  $\Sigma_{xy}^{vis}$  which monotonically increases with increasing Ca.

The trends of  $|N_1^{vis}|$  and  $N_2^{vis}$  versus Ca can be partly explained based on the isotropic model. Using Eq. (19) we can evaluate  $N_1^{vis,geom}$  and  $N_2^{vis,geom}$  for oblate spheroids for different values of aspect ratio  $\alpha$  and inclination angle  $\theta$ . It appears that  $|N_1^{vis,geom}|$  and  $N_2^{vis,geom}$  are maximum at  $\theta = \pi/4$ , and they decrease with decreasing  $\theta$  and  $\alpha$ . In the limits of  $\alpha \rightarrow 1$  (i.e.,  $Ca \rightarrow 0$ ), and  $\theta \rightarrow 0$  ( $Ca \rightarrow \infty$ ), both  $N_1^{vis,geom}$  and  $N_2^{vis,geom}$  vanish. Then, the maximum values of  $|N_1^{vis,geom}|$  and  $N_2^{vis,geom}$  (and, hence,  $|N_1^{vis}|$  and  $N_2^{vis}$ ) occur at intermediate values of Ca. As a result,  $N_1^{vis}$  and  $N_2^{vis}$  exhibit nonmonotonic trends with Ca.

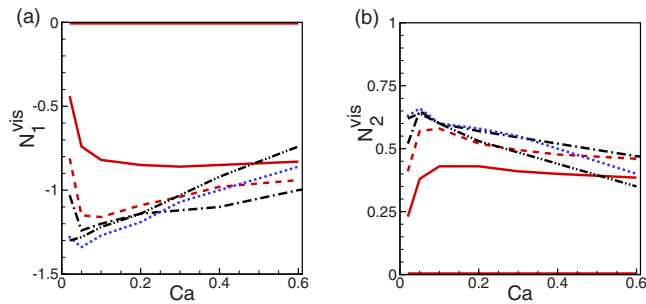


FIG. 17. (Color online) Effect of Ca on the viscous contributions (a)  $N_1^{vis}$ , and (b)  $N_2^{vis}$  for SK model with  $C=1$ . Line patterns represent different values of  $\lambda$  as in Fig. 11.  $\lambda=1$  (thick red lines), 3 (thin red lines), 5 (dash red lines), 7 (black dash-dot lines), 10 (blue dotted lines), and 13 (black dash-dot-dot lines).

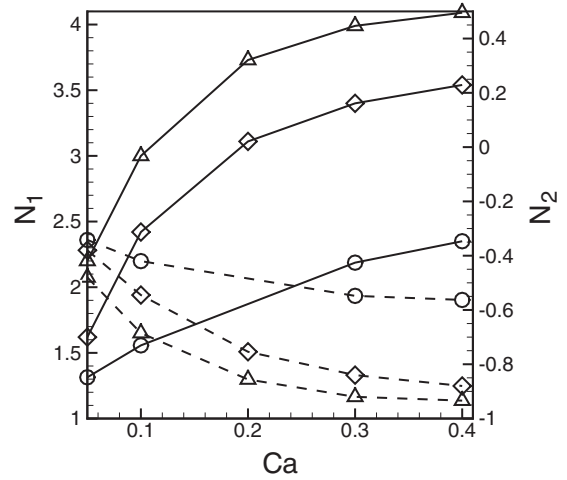


FIG. 18. Effect of area dilatation on  $N_1$  (continuous line, left axis) and  $N_2$  (dash lines, right axis). Variation with respect to Ca is shown at  $\lambda=1$ . Symbols represent NH model ( $\Delta$ ), and SK models with  $C=0.1$  ( $\diamond$ ), and 50 ( $\circ$ ).

Effect of area dilatation on the normal stress differences is shown in Fig. 18 by considering three cases: the NH model, and the SK model with  $C=0.1$ , and 50. For all cases,  $N_1$  and  $|N_2|$  increase nonlinearly with increasing Ca. As expected,  $N_1 > 0$ ,  $N_2 < 0$ , and  $N_1 > |N_2|$ , for all cases. However,  $N_1$  and  $|N_2|$  decrease with increasing  $C$  due to reduced capsule deformation. Thus the elastic nature of the bulk suspension is reduced with decreasing area dilatation of the membrane.

#### IV. SUMMARY

We present numerical results on the rheology of a dilute suspension of elastic capsules in linear shear flow. We show that a shear viscosity minimum exists for the capsule suspensions. However, unlike a vesicle suspension, the capsule suspension exhibits the shear viscosity minimum even when the capsules are in a steady tank-treading motion. This anomaly is explained by decomposing the particle stress into elastic and viscous components. It is shown that the elastic component is shear thinning, but the viscous component is shear thickening. Such opposite trends are responsible for the shear viscosity minimum in a capsule suspension. These trends are qualitatively explained based on an isotropic model. The shear viscosity minimum is observed for area-dilating membranes but not for nearly incompressible membranes. This result is in stark contrast to that of the vesicle suspension because the vesicle surface is incompressible.

The normal stress differences  $N_1$  and  $N_2$  show much more complex trends. At low viscosity ratio, their magnitudes increase with increasing Ca. But this trend is completely reversed at high viscosity ratio. Further,  $N_1$  and  $|N_2|$  decrease uniformly with increasing  $\lambda$ , in a stark departure from the predictions of the small-deformation theory. The elastic and viscous components of  $N_1$  and  $N_2$  are analyzed to explain the observed trends. It is shown that the viscous components can be described by the isotropic model, but the elastic components depend strongly on anisotropic distribution of the membrane tension.

We note that no shape change is possible for a volume- and surface-area preserving object with a spherical initial shape. Thus, a vesicle has an excess area to start with. In contrast, the area of an initially spherical capsule is allowed to dilate in order for it to deform. However, a nonspherical capsule can change its shape without area dilatation. Thus, it would be of interest to extend our simulations to nonspherical capsules with nearly incompressible membranes. It would be of interest also to study the effect of unsteady dynamics of nonspherical capsules on the time-dependent

rheology of the suspension. Finally, it would be interesting to consider dense or semidense suspensions of multiple capsules.

#### ACKNOWLEDGMENTS

This work was funded by NSF Grant Nos. BES-0603035 and CTS-0625936. Computational supports from the NSF-funded Teragrid resources at TACC, NCSA, and NERSC resources at DOE LBNL are acknowledged.

- 
- [1] A. S. Popel and P. C. Johnson, *Annu. Rev. Fluid Mech.* **37**, 43 (2005).
- [2] R. Fahraeus and T. Lindqvist, *Am. J. Physiol.* **96**, 562 (1931).
- [3] H. L. Goldsmith, G. R. Cokelet, and P. Gaetgens, *Am. J. Physiol.* **257**, H1005 (1989).
- [4] A. R. Pries, D. Neuhaus, and P. Gaetgens, *Am. J. Physiol.* **263**, H1770 (1992).
- [5] E. R. Damiano, D. S. Long, and M. L. Smith, *J. Fluid Mech.* **512**, 1 (2004).
- [6] Q. Zhu, C. Vera, R. J. Asaro, P. Sche, and L. A. Sung, *Biophys. J.* **93**, 386 (2007).
- [7] N. Mohandas and E. Evans, *Annu. Rev. Biophys. Biomol. Struct.* **23**, 787 (1994).
- [8] H. L. Goldsmith, *Fed. Proc.* **30**, 1578 (1971).
- [9] H. Goldsmith and J. Marlow, *Proc. R. Soc. London, Ser. B* **182**, 351 (1972).
- [10] T. M. Fischer, M. Stohr-Liesen, and H. Schmid-Schonbein, *Science* **202**, 894 (1978).
- [11] R. Tran-Son-Tay, Ph.D. thesis, Washington University, 1983.
- [12] M. Abkarian, M. Faivre, and A. Viallat, *Phys. Rev. Lett.* **98**, 188302 (2007).
- [13] T. M. Fischer, *Biophys. J.* **93**, 2553 (2007).
- [14] S. R. Keller and R. Skalak, *J. Fluid Mech.* **120**, 27 (1982).
- [15] Y. Sui, Y. T. Chew, P. Roy, Y. P. Cheng, and H. T. Low, *Phys. Fluids* **20**, 112106 (2008).
- [16] H. Rehage, M. Husmann, and A. Walter, *Rheol. Acta* **41**, 292 (2002).
- [17] S. Ramanujan and C. Pozrikidis, *J. Fluid Mech.* **361**, 117 (1998).
- [18] J. M. Skotheim and T. W. Secomb, *Phys. Rev. Lett.* **98**, 078301 (2007).
- [19] Y. Sui, H. T. Low, Y. T. Chew, and P. Roy, *Phys. Rev. E* **77**, 016310 (2008).
- [20] S. Kessler, R. Finken, and U. Seifert, *J. Fluid Mech.* **605**, 207 (2008).
- [21] P. Bagchi and R. M. Kalluri, *Phys. Rev. E* **80**, 016307 (2009).
- [22] V. Kantsler and V. Steinberg, *Phys. Rev. Lett.* **95**, 258101 (2005).
- [23] V. Kantsler and V. Steinberg, *Phys. Rev. Lett.* **96**, 036001 (2006).
- [24] H. Noguchi and G. Gompper, *Phys. Rev. Lett.* **98**, 128103 (2007).
- [25] M.-A. Mader, V. Vitkova, M. Abkarian, A. Viallat, and T. Podgorski, *Eur. Phys. J. E* **19**, 389 (2006).
- [26] J. Deschamps, V. Kantsler, and V. Steinberg, *Phys. Rev. Lett.* **102**, 118105 (2009).
- [27] F. Rioual, T. Biben, and C. Misbah, *Phys. Rev. E* **69**, 061914 (2004).
- [28] C. Misbah, *Phys. Rev. Lett.* **96**, 028104 (2006).
- [29] P. M. Vlahovska and R. S. Gracia, *Phys. Rev. E* **75**, 016313 (2007).
- [30] G. Danker, T. Biben, T. Podgorski, C. Verdier, and C. Misbah, *Phys. Rev. E* **76**, 041905 (2007).
- [31] H. Noguchi and G. Gompper, *Phys. Rev. Lett.* **93**, 258102 (2004).
- [32] H. Noguchi and G. Gompper, *Phys. Rev. E* **72**, 011901 (2005).
- [33] M.-A. Mader, H. Ez-Zahraouy, C. Misbah, and T. Podgorski, *Eur. Phys. J. E* **22**, 275 (2007).
- [34] V. V. Lebedev, K. S. Turitsyn, and S. S. Vergeles, *New J. Phys.* **10**, 043044 (2008).
- [35] V. V. Lebedev, K. S. Turitsyn, and S. S. Vergeles, *Phys. Rev. Lett.* **99**, 218101 (2007).
- [36] G. K. Batchelor, *J. Fluid Mech.* **41**, 545 (1970).
- [37] D. Barthes-Biesel and V. Chhim, *Int. J. Multiphase Flow* **7**, 493 (1981).
- [38] C. Pozrikidis, *J. Fluid Mech.* **297**, 123 (1995).
- [39] C. Pozrikidis, *Ann. Biomed. Eng.* **31**, 1194 (2003).
- [40] G. Danker and C. Misbah, *Phys. Rev. Lett.* **98**, 088104 (2007).
- [41] G. Danker, C. Verdier, and C. Misbah, *J. Non-Newtonian Fluid Mech.* **152**, 156 (2008).
- [42] V. Vitkova, M.-A. Mader, B. Polack, C. Misbah, and T. Podgorski, *Biophys. J.* **95**, L33 (2008).
- [43] G. Tryggvason, B. Bunner, A. Esmaeeli, N. Al-Rawahi, W. Tauber, J. Han, S. Nas, and Y. Jan, *J. Comput. Phys.* **169**, 708 (2001).
- [44] S. O. Unverdi and G. Tryggvason, *J. Comput. Phys.* **100**, 25 (1992).
- [45] C. S. Peskin, *J. Comput. Phys.* **25**, 220 (1977).
- [46] L. A. Miller and C. S. Peskin, *J. Exp. Biol.* **208**, 195 (2005).
- [47] S. K. Doddi and P. Bagchi, *Phys. Rev. E* **79**, 046318 (2009).
- [48] S. K. Doddi and P. Bagchi, *Int. J. Multiphase Flow* **34**, 966 (2008).
- [49] R. Skalak, A. Tozeren, P. R. Zarda, and S. Chien, *Biophys. J.* **13**, 245 (1973).
- [50] E. Lac, A. Morel, and D. Barthes-Biesel, *J. Fluid Mech.* **573**, 149 (2007).
- [51] X. Li and K. Sarkar, *J. Comput. Phys.* **227**, 4998 (2008).
- [52] G. I. Taylor, *Proc. R. Soc. London, Ser. A* **138**, 41 (1932).
- [53] P. Vlahovska, J. Blawdziewicz, and M. Loewenberg, *J. Fluid Mech.* **463**, 1 (2002).